Moving Dirac nodes by chemical substitution

Niloufar Nilforoushan[1], Michele Casula[2], Adriano Amaricci[3,4], Marco Caputo[1,5], Jonathan Caillaux[1], Lama Khalil[1,6], Evangelos Papalazarou[1], Pascal Simon[1], Luca Perfetti[7], Ivana Vobornik[3], Pranab Kumar Das[3,8], Jun Fuji[3], Alexei Barinov[3], David Santos-Cottin[2], Yannick Klein[2], Michele Fabrizio[4], Andrea Gauzzi[2], and Marino Marsi[1]

[1]Université Paris-Saclay, CNRS, Laboratoire de Physique des Solides,91405 Orsay, France.; [2]Institut de Minéralogie, de Physique des Matériaux et de Cosmochimie (IMPMC), Sorbonne Université, CNRS UMR 7590, MNHN, 4 place Jussieu, 75252 Paris, France.; [3]Istituto Officina dei Materiali (IOM) - CNR, Strada Statale 14 km 163.5, 34149 Trieste, Italy.; [4]International School for Advanced Studies SISSA, via Bonomea 265, 34136 Trieste, Italy.; [5]Sincrotrone Trieste, SS14 - Km 163.5, 34149 Trieste, Italy.; [6]Synchrotron SOLEIL, Saint Aubin BP 48, Gif-sur-Yvette, F-91192, France; [7]Laboratoire des Solides Irradiés, Ecole Polytechnique, CNRS, CEA, 91128 Palaiseau, France.; [8]International Centre for Theoretical Physics, Strada Costiera 11, 34100 Trieste, Italy.

This manuscript was compiled on November 30, 2021

Dirac fermions play a central role in the study of topological phases, for they can generate a variety of exotic states, such as Weyl semimetals and topological insulators. The control and manipulation of Dirac fermions constitute a fundamental step towards the realization of novel concepts of electronic devices and quantum computation. By means of ARPES experiments and *ab initio* simulations, here we show that Dirac states can be effectively tuned by doping a transition metal sulfide, $BaNiS_2$, through Co/Ni substitution. The symmetry and chemical characteristics of this material, combined with the modification of the charge transfer gap of $BaCo_{1-x}Ni_xS_2$ across its phase diagram, lead to the formation of Dirac lines whose position in k-space can be displaced along the $\Gamma - M$ symmetry direction, and their form reshaped. Not only does the doping x tailor the location and shape of the Dirac bands, but it also controls the metal-insulator transition in the same compound, making $BaCo_{1-x}Ni_xS_2$ a model system to functionalize Dirac materials by varying the strength of electron correlations.

Dirac semimetals | Correlated electronic systems | Functional topological materials

In the vast domain of topological Dirac and Weyl materials (1–9), the study of various underlying mechanisms (10–15) leading to the formation of non-trivial band structures is key to discover new topological electronic states (16–23). A highly desirable feature of these materials is the tunability of the topological properties by an external parameter, which will make them suitable in view of technological applications, such as topological field effect transistors (24). While a thorough control of band topology can be achieved in principle in optical lattices (25) and photonic crystals (26) through the wandering, merging and reshaping of nodal points and lines in **k**-space (27, 28), in solid state systems such a control is much harder to achieve. Proposals have been made by using optical cavities (29), twisted van der Waals heterostructures (30), intercalation (31), chemical deposition (32, 33), impurities (34), and magnetic and electric applied fields (35), both static (36) and time-periodic (17, 37). Here, we prove that it is possible to move and reshape Dirac nodal lines in reciprocal space by chemical substitution. Namely, by means of Angle Resolved Photo-Emission Spectroscopy (ARPES) experiments and *ab initio* simulations, we observe a sizable shift of robust massive Dirac nodes towards Γ in $BaCo_{1-x}Ni_xS_2$ as a function of doping x, obtained by replacing Ni with Co. At variance with previous attempts of controlling Dirac states by doping (19, 38), in our work we report both a reshape and a significant **k**-displacement of the Dirac nodes.

$BaCo_{1-x}Ni_xS_2$ is a prototypical transition metal system with a simple square lattice (39). In $BaCo_{1-x}Ni_xS_2$ the same doping parameter x that tunes the position of the Dirac nodes also controls the electronic phase diagram, which features a first-order metal-insulator transition (MIT) at a critical substitution level, $x_{cr} \sim 0.22$ (40, 41), as shown in Fig. 1(a). The Co-rich side ($x = 0$) is an insulator with collinear magnetic order and with local moments in a high-spin (S=3/2) configuration (42). Both electron correlation strength and charge-transfer gap Δ_{CT} increase with decreasing x, as typically found in the late transition metal series. The MIT at $x = 0.22$ is of interest because it is driven by electron correlations (43) and is associated with a competition between an insulating antiferromagnetic phase and an unconventional paramagnetic semi-metal (44), where the Dirac nodes are found at the Fermi level. We show that a distinctive feature of these Dirac states is their dominant d-orbital character and that the underlying band inversion mechanism is driven by a large $d - p$ hybridization combined with the non-symmorphic symmetry (NSS) of the crystal (see Fig. 1(b)). It follows that an essential role in controlling the properties of Dirac states is played by electron correlations and by the charge-transfer gap (Fig. 1 (c)), as they have a direct impact on the hybridization strength. This results into an effective tunability of shape, energy and wave vector of the Dirac lines in the proximity of the Fermi level. Specifically, the present ARPES study unveils Dirac bands moving from M to Γ with decreasing x. The bands are well explained quantitatively by *ab initio* calcula-

Significance Statement

The on-demand control of topological properties with readily modifiable parameters is a fundamental step towards the design of novel electronic and spintronic devices. Here we show that this goal can be achieved in the correlated system $BaCo_{1-x}Ni_xS_2$, where we succeeded in significantly changing the reciprocal space position and shape of Dirac nodes by chemically substituting Ni with Co. We prove that the tunability of the Dirac states is realized by varying the electron correlation strength and the charge-transfer gap, both sensitive to the substitution level, x. Based on our finding, a class of late transition metal compounds can be established as prototypical for engineering highly tunable Dirac materials.

authors contribution: N.N., M.Cas., M.F., A.G. and M.M. designed research; N.N., M.Cas., A.A., M.Cap., J.C., L.K., E.P., P.S., L.P., I.V., P.K.D., J.F., A.B., D.S.C., Y.K., M.F., A.G. and M.M. performed research; N.N., M.Cas., A.A., M.F. and M.M. analyzed data; N.N., M.Cas., A.A.,M.F., A.G. and M.M. wrote the paper.

author declaration: xxx.

To whom correspondence should be addressed. E-mail:niloufar.nilforoushan@phys.ens.fr ; michele.casula@sorbonne-universite.fr ; marino.marsi@universite-paris-saclay.fr

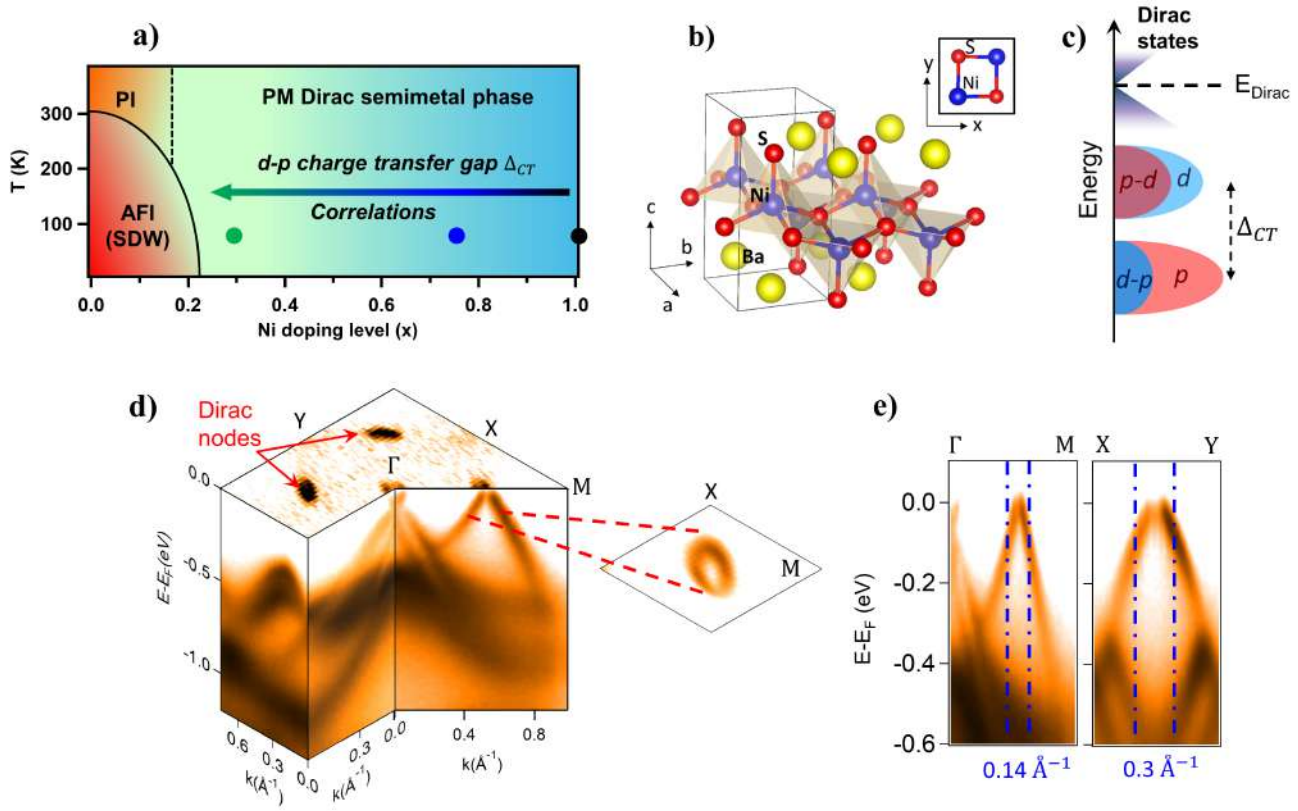

Fig. 1. Experimental observation of Dirac states in the phase diagram of $BaCo_{1-x}Ni_xS_2$. (a) Phase diagram of $BaCo_{1-x}Ni_xS_2$. The transition lines between the paramagnetic metal (PM), the paramagnetic insulator (PI), and the antiferromagnetic insulator (AFI) are reported. Colored circles indicate the different doping levels x studied in this work. This doping alters the $d-p$ charge transfer gap (Δ_{CT}). (b) Crystal structure of $BaNiS_2$. Blue, red and yellow spheres represent the Ni, S and Ba atoms, respectively. The tetragonal unit cell is indicated by black solid lines. Lattice parameters are a = 4.44 Å and c = 8.93 Å(45). Top: projection of the unit cell in the xy plane, containing two Ni atoms. (c) Schematics of the energy levels. The hybridization of $d-$ and $p-$ orbitals creates the Dirac states, and the $d-p$ charge transfer gap fixes the position of these states in the $E-k$ space. (d) A three-dimensional ARPES map of $BaNiS_2$ ($x=1$) taken at 70 eV photon energy. The top surface shows the Fermi surface and the sides of the cube present the band dispersion along high-symmetry directions . The linearly dispersing bands along $\Gamma-M$ cross each other at the Fermi level, E_F, thus creating four Dirac nodes. (e) We observe the oval-shaped section of the linearly dispersing bands on the k_x-k_y plane for $E-E_F=-100$ meV. The linearly dispersing bands along the major and minor axis of the oval are also shown.

tions, in a hybrid density functional approximation suitable for including non-local correlations of screened-exchange type, which affect the hybridization between the d and p states. The same functional is able to describe the insulating spin-density wave (SDW) phase at $x=0$, driven by local correlations, upon increase of the optimal screened-exchange fraction. These calculations confirm that the Dirac nodes mobility in **k**-space stems directly from the evolution of the charge transfer gap, i.e. the relative position between d and p on-site energies. These results clearly suggest that $BaCo_{1-x}Ni_xS_2$ is a model system to tailor Dirac states and, more generally, that two archetypal features of correlated systems such as the hybrid $d-p$ bands and the charge-transfer gap constitute a promising playground to engineer Dirac and topological materials using chemical substitution and other macroscopic control parameters.

Observation of Dirac states in $BaNiS_2$

We begin with the undoped sample $BaNiS_2$. In Fig. 1(d), we represent a three dimensional ARPES map of the Brillouin zone (BZ) for the high symmetry directions. Along $\Gamma-M$, we observe linearly dispersing bands and -within ARPES resolution- gapless nodes at the Fermi level E_F. The Fermi surface reveals two pairs of such Dirac-like crossings related to each other by the time-reversal and by the two-fold rotation axis C_2 of the C_{2v} little group for the **k**-vectors along $\Gamma-M$. The Dirac nodes lie on the σ_d reflection planes and extend along the k_z direction piercing the whole BZ, unlike other topological node-line semimetals known to date, like Cu_3NPd (46, 47), Ca_3P_2 (48) and ZrSiS (49), where the nodal lines form closed areas around high-symmetry points.

As one can see in Fig. 1(e), along the $\Gamma-M$ direction, the linearly dispersing bands remain isolated up to about $E-E_F=-0.35$ eV. These bands create an oval-shaped section on the constant energy maps near the Fermi level (see Fig. 1(d)). This asymmetry, clearly visible in Fig. 1(e), arises from the tilted type-I nature of the Dirac cone. The model Hamiltonian explaining the low-energy spectrum of the linearly dispersing bands observed experimentally is described

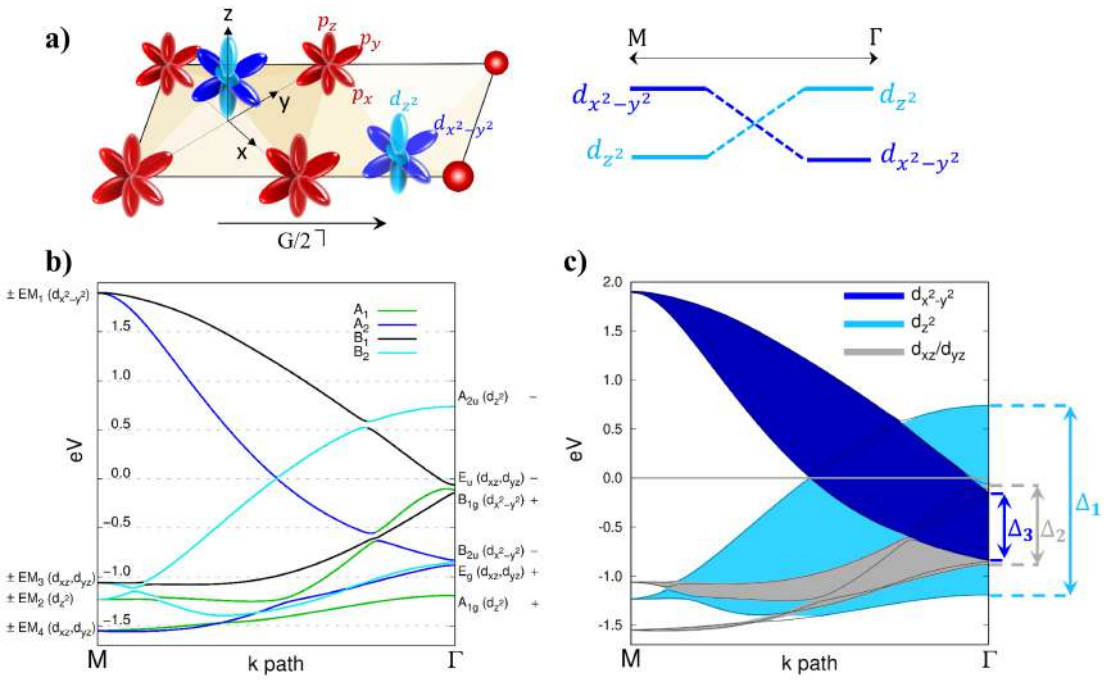

Fig. 2. Mechanism of band inversion and formation of hybridized Dirac states. (a) Schematics of the d- and p-orbitals of Ni and S, respectively. Right panel: The strong hybridization of the d-orbitals with the ligand p-orbitals, favored by the NSS, is responsible for the band inversion. (b) Band symmetries along the MΓ direction. At the right (left) -hand side of the panel, we report the symmetries at Γ (M), while the symmetries in between follow the irreducible representations of the C_{2v} point group, represented by the color code in the key. The outer $+/-$ signs indicate the parity of the respective Bloch wave functions at the beginning and at the end of the **k**-path. (c) Evolution of the energy splitting between even and odd combinations of d-orbitals along MΓ. The dominant orbital character is reported. The navy blue (blue) vertical arrows indicate the splitting Δ_3 (Δ_1) between the $d_{x^2-y^2}$ (d_{z^2}) bands at Γ due to the hybridization with the ligand p_z-orbitals. The grey arrow indicates the splitting Δ_2 of d_{xz}/d_{yz} bands at Γ due to their hybridization with the p_x/p_y orbitals.

in the Supporting Information (SI), c.f. Sec. S1. The linear bands present no k_z dispersion, as shown in the SI (Sec. S2 and Fig. S2). The absence of dispersion is an indication of the 2D nature of the Dirac cones. The Dirac point remains pinned almost at the Fermi level - about 30 meV above - and its wave vector is fixed along the $\Gamma(Z) - M(A)$ direction. Here, the Dirac point position is obtained by extrapolating the ARPES data. These values are in perfect agreement with those directly measured in a recent pump-probe experiment (50).

Symmetry analysis of the electronic bands: mechanism of band inversion and formation of Dirac states

To unveil the physical mechanism responsible for the formation of Dirac cones in $BaNiS_2$ we performed a detailed theoretical analysis of the symmetry of the electronic bands. We carried out density functional theory (DFT) calculations, by employing a modified Heyd–Scuseria–Ernzerhof (HSE) functional. The details of the band structure are presented in Methods and SI (see SI Sec. S3, where we also discuss how the inclusion of the spin-orbit coupling (SOC) affects the topological properties). The use of the HSE functional is dictated by non-local correlation effects present in this material. Indeed, a hybrid HSE functional with the optimal screened-exchange fraction $\alpha = 7\%$ (see Eq. 1) is needed to account for the Fermi surface renormalization of $BaNiS_2$ seen in quantum oscillations (51). Previous theoretical calculations (41, 52, 53) have shown that both S 3p- and Ni 3d-orbitals contribute to the Bloch functions near the Fermi level. We ascribe the electronic states close to the Fermi level mainly to the Ni 3d-orbitals hybridized with the S 3p-orbitals. In this situation, the exchange contribution to the hybridization with the ligands plays a crucial role in determining the topology of the Fermi surface (Fig. S6(b) illustrates the electronic structure dependence upon α). Hereafter, we consider a Cartesian reference frame where the x- and y-axis are parallel to the Ni-S bonds in the tetragonal ab-plane. Neighbouring Ni ions are aligned along the diagonal xy direction (Fig. 1(b)). In this frame, at the crossing points, located along the (u, u, v) directions, the bands have dominant d_{z^2} and $d_{x^2-y^2}$ character. This multi-orbital nature was confirmed by a polarization dependent laser-ARPES study (see SI, Sec. S4).

As sketched in Fig. 2(a), the crystal structure of $BaNiS_2$ is made of square-lattice layers of staggered, edge-sharing NiS_5 pyramids pointing along the out-of-plane [001] c-axis direction (40). The Ni atoms inside the S pyramids probe a crystal field that splits the atomic d-shell into the following levels (in descending energy order): $d_{x^2-y^2}$, d_{z^2}, the degenerate doublet (d_{xz}, d_{yz}) and d_{xy}. Due to the $3d^8 4s^0$ electronic configuration of the Ni^{2+} ion, we expect all d-orbitals to be filled, except the two highest ones, $d_{x^2-y^2}$ and d_{z^2}, which are nearly half-filled assuming that the Hund's exchange is sufficiently strong.

The puckering of the $BaNiS_2$ layers gives rise to a tetragonal nonsymmorphic $P4/nmm$ structure characterized by a horizontal gliding plane which generates two Ni and two apical S positions at (1/4,1/4,z) and (3/4,3/4,$-z$), separated by a fractional $\mathbf{f}$=(1/2,1/2,0) translation in the plane, Fig. 2(a). The two Ni atoms occupy Wyckoff position 2c, corresponding to the M symmetry, while the two planar S are at the 2a site corresponding to the Γ symmetry.

At M, the energy hierarchy of the atomic orbitals follows closely the crystal field splitting (Fig. 2(b)). The little group admits the following four 2D irreducible representations (irreps) $E_{Mi=1,...,4}$ (54), each originating from the same orbitals of the two inequivalent Ni. However, the levels stacking at Γ, whose little group is isomorphic to D_{4h}, differs from that predicted by the crystal field. This is due to the sizable hybridization of Ni d-orbitals with the S p ligands (see SI, Sec. S5). Owing to the NSS, each Bloch eigenfunction at Γ is either even or odd upon exchanging the inequivalent Ni and S within each unit cell. Even and odd combinations of identical d-orbitals belonging to inequivalent Ni atoms split in energy since they hybridize differently with the ligands. The even combination of the $d_{x^2-y^2}$ Ni orbitals is weakly hybridized with the p_z-orbitals of the planar S, since the two Ni atoms are out of the basal plane. On the other hand, the odd combination is non-bonding. It follows that the B_{1g} even combination shifts up in energy with respect to the B_{2u} odd one. Seemingly, the A_{2u} odd combination of the d_{z^2}-orbitals hybridizes substantially with the p_z-orbitals of the planar and apical S, thus increasing significantly the energy of the odd combination. Eventually, its energy raises above the B_{1g} and B_{2u} levels, as well as the A_{1g} state (even combination of d_{z^2}-orbitals). This leads to a reverse of the crystal field order as reported in Fig. 2(c).

Because the irreps at the A and Z $\mathbf{k}$-points are equivalent to those at M and Γ (54), respectively, the orbital hierarchy found at M and Γ must be preserved along the $M-A$ and $\Gamma-Z$ directions. Thus, for any v along the $(0,0,v) \rightarrow (1/2,1/2,v)$ path, a band inversion between bands with predominant d_{z^2} and $d_{x^2-y^2}$ characters must occur. Therefore, band crossing is allowed without SOC, and leads to two Dirac points at a given k_z right at the Fermi energy for $k_z = 0$. Indeed, the crossing bands transform like different irreps of the little group, which is isomorphic to C_{2v} for a $\mathbf{k}$-point (u,u,v) with $v = 0, 1/2$, and to C_s with $v \in]0,1/2[$. These Dirac nodes are massive as a consequence of the SOC, which makes the material a weak topological insulator. The SOC gap is however very small (about 18 meV), and below ARPES resolution. Nevertheless, the focus of the present work is not on these very-low-energy features, but rather on the tunability of the whole Dirac nodal structure. In the family of weak topological insulators having the same $P4/nmm$ space group and showing SOC gapped Dirac cones along the $\Gamma - M$ direction (such as ZrSiS, for instance), $BaCo_{1-x}Ni_xS_2$ is a peculiar member. Indeed, the strong local Hund's exchange coupling favors nearly half-filled $d_{x^2-y^2}$ and d_{z^2} orbitals, that explains the proximity of the Dirac nodes to the Fermi level for $x = 1$, in accordance also to Luttinger's theorem (see SI, Sec. S6). This is another signature of the relevance of electron correlations in this transition metal compound, which manifest themselves in both local and non-local contributions, the former leading eventually to the insulating phase at the Co side of $BaCo_{1-x}Ni_xS_2$, the latter affecting the variation of Δ_{CT} across the series.

ARPES evidence of Dirac states tuned by doping, x

We now turn our attention to the effect of the Co/Ni substitution on the evolution of the band structure, notably the Dirac states. According to the $BaCo_{1-x}Ni_xS_2$ phase diagram, this substitution modifies the strength of the electron-electron correlations and the amplitude of Δ_{CT}. A series of ARPES spectra are given for the $x = 0.75$ and $x = 0.3$ compositions. In Fig. 3, we display the evolution of the Fermi surface and the electronic band structure along $\Gamma - M$ with x. For $x = 0.75$, the Fermi surface is composed of a four-leaf feature at the Γ point and four hole-like pockets along the $\Gamma - M$, Fig. 3(c). These pockets originate from the Dirac states crossing the Fermi level. The Dirac cone is shown in Fig. 3(d) along and perpendicular to the $\Gamma - M$ direction. At higher substitution levels, for $x = 0.30$, the Dirac states shift up to lower binding energies, so the size of the hole-like pockets in the $k_x - k_y$ plane is increased (see Fig. 3(e,f)). The ARPES signal is also broader: since our structural study indicates that the crystalline quality is not affected by Co/Ni substitution (see Sec. S7 and Tab. S2 in SI), this broadening is consistent with the increase in electron-electron correlations while approaching the metal-insulator transition. (39, 43, 52). On the theoretical ground, this is expected because Co-substitution brings the whole d-manifold closer to fillings where local correlation effects are enhanced, according to the Hund's metals picture (55). Fig. 4(a) schematically illustrates the evolution of the Dirac cone with x; in Table 1 we give the position of the Dirac points determined by extrapolating the band dispersion. In summary, one notes that the Co-substitution moves the Dirac points further beyond the Fermi level and reduces its wave vector.

Table 1. Position of the Dirac point (DP) in energy and momentum space for different doping levels in the metallic phase.

Compound	E_{DP} (eV)	k_{DP}(Å^{-1})
$BaNiS_2$	0.03± 0.01	0.52± 0.01
$BaCo_{0.25}Ni_{0.75}S_2$	0.19± 0.01	0.49± 0.01
$BaCo_{0.7}Ni_{0.3}S_2$	0.37± 0.02	0.39± 0.02

Evolution of Dirac states with doping

In order to account for the tunability of the Dirac cones detected by ARPES, we carried out extensive *ab initio* DFT-HSE calculations as a function of the screened-exchange fraction α, which controls the correlation strength in the modified hybrid functional framework. To explicitly include the charge transfer Δ_{CT} variation led by chemical substitution, we computed the two end-members of the $BaCo_{1-x}Ni_xS_2$ series, namely $x = 1$ ($BaNiS_2$) and $x = 0$ ($BaCoS_2$). For $x = 1$ the optimal $\alpha = 7\%$, since it reproduces the frequencies of quantum oscillations in $BaNiS_2$ (51). In order to fix such percentage for $x = 0$, we performed *ab initio* calculations assuming the collinear SDW observed experimentally (42), by means of both HSE and the generalized gradient approximation supplemented by local Hubbard interactions (GGA+U). The strength of the Hubbard repulsion $U = 3.0$ eV and local Hund's coupling $J = 0.9$ eV, included in GGA+U, was estimated from first principles within the constrained random phase approximation

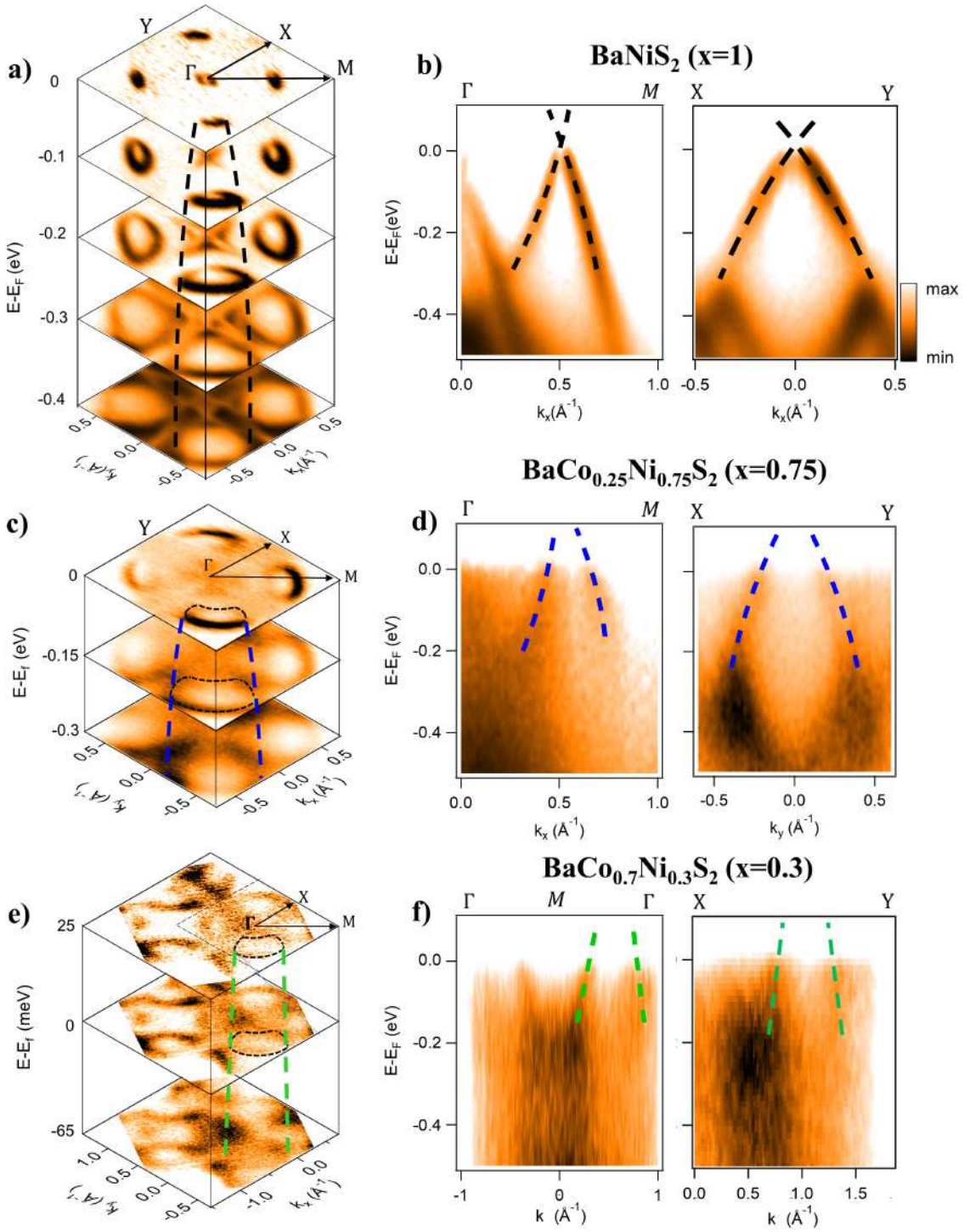

Fig. 3. Experimental ARPES evolution of Dirac states with doping x, in $BaCo_{1-x}Ni_xS_2$. (a, b) Dispersion of these states for $x = 1$. Panel (a) shows the iso-energy contours with increasing binding energy. Panel (b) shows the dispersion along the high symmetry directions $\Gamma - M$ and $X - X'$. Note the anisotropy of the dispersion, which is due to the oval shape of the pockets at the Fermi surface. Dashed lines are a guide to the eye that represent schematically the dispersion. (c-d) and (e-f): the same as in panels (a-b) for the $x = 0.75$ and the $x = 0.3$ samples, respectively. All spectra are obtained with a photon energy of 70 eV.

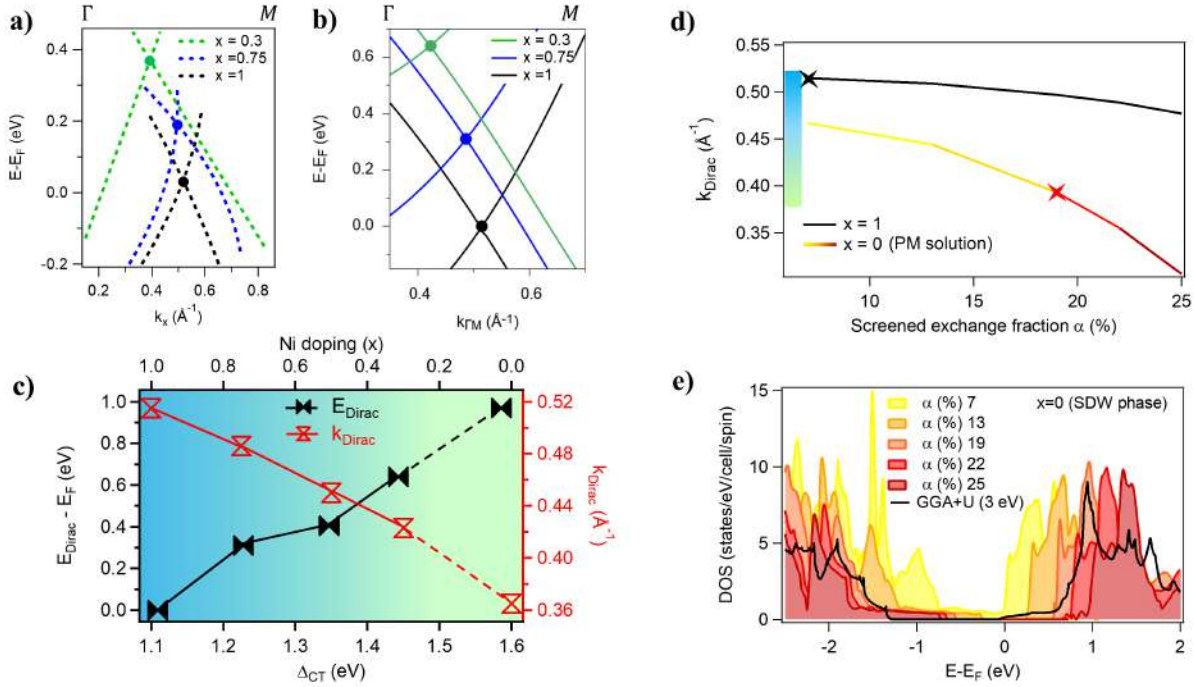

Fig. 4. Evolution of Dirac states with doping x, in $BaCo_{1-x}Ni_xS_2$. (a) Curves fitting the experimental Dirac states for different values of x. (b) Evolution of the Dirac states predicted by our HSE/tight-binding calculations of the band structure. (c) Variation of the charge transfer gap, $\Delta_{\rm CT}$, with the Ni content, x. The point at $x = 0$ is the metastable state adiabatically connected with the metallic phase found for $x > x_{cr} \simeq 0.22$. By reducing x from 1 to 0, the Dirac point, $\mathbf{k}_{\rm Dirac}$, moves towards Γ. Correspondingly, the difference between the energy of this point and the Fermi level increases. (d) $\mathbf{k}_{\rm Dirac}$ variation for $x = 0$ and $x = 1$, when we relax the screened-exchange fraction parameter α in the modified HSE functional. The black (red) star is located at the value of α that optimally captures the correlation strength in $BaNiS_2$ ($BaCoS_2$), used to predict the evolution in panels (b) and (c). (e) Density of states (DOS) of the $x = 0$ collinear SDW solution, as computed by GGA+U (black line) with *ab initio* values for the local Hubbard repulsion, and the modified HSE with values for α covering different correlation strengths. Optimal $\alpha = 19\%$ best matches the GGA+U DOS.

(43). GGA+U correctly predicts an insulating state (Fig. 4(e)). By varying the percentage α of screened exchange in HSE, we find that, while $\alpha = 7\%$ gives a metal, $\alpha \simeq 19\%$ reproduces the main peaks across gap obtained by GGA+U (Fig. 4(e)). This result suggests that HSE can describe $BaCo_{1-x}Ni_xS_2$ only if the percentage of screened exchange α increases from 7% up to around 19% with decreasing x from 1 to 0. Starting from the most correlated Co side, the reduction of the Hubbard repulsion upon electron doping, implied by the α dependence on x, has been found in other strongly correlated compounds, such as La-doped Sr_2IrO_4 (56).

In $BaCoS_2$, beside the SDW solution compatible with the observed low-temperature state, it is possible to obtain another one once magnetism is not allowed, namely forcing spin $SU(2)$ symmetry. This paramagnetic metallic (PM) phase is metastable at low temperature, and adiabatically connected with the metallic solution at $x = 1$. Therefore, it hosts Dirac cones; it is metallic and separated by an energy barrier from the stable insulating SDW phase. In Fig. 4(d), we plot the distance of the Dirac node ($\mathbf{k}_{\rm Dirac}$) from the Γ point as a function of α, for $x = 1$ and the metallic solution at $x = 0$. $\mathbf{k}_{\rm Dirac}$ strongly depends on both x and α (See sec. S8, Figs. S6(a) and S6(b) plot the band structures where the $\mathbf{k}_{\rm Dirac}$ values have been extracted from). By taking the optimal α's for each x, the Dirac node is predicted to drift from $\mathbf{k}_{\rm Dirac} \simeq 0.52\,\text{Å}^{-1}$ at $x = 1$ down to $\mathbf{k}_{\rm Dirac} \simeq 0.38\,\text{Å}^{-1}$ at $x = 0$, covering the colored y-axis range in Fig. 4(d), in agreement with the range of variation seen in experiment.

Next, we analyze the 22-bands full $d-p$ tight-binding model derived from the *ab initio* DFT-HSE for $x = 1$ (with $\alpha = 7\%$) and for $x = 0$ (with $\alpha = 19\%$), c.f. Sec. S9, and Fig. S8 The $x = 0$ state has shifted Dirac cones in both $\mathbf{k}$ and energy position with respect to the $BaNiS_2$ parent compound. To underpin the mechanism behind the evolution of the cones, we compared the two tight-binding Hamiltonians for $x = 0$ and $x = 1$ The main difference involves the on-site energies and, in particular, the relative position of the p and d states, i.e. the charge transfer gap Δ_{CT}. This proves that the doping x via chemical substitution is indeed an effective control parameter, as it alters the $d-p$ charge transfer gap Δ_{CT} together with the

correlation strength and, consequently, the $d-p$ hybridization amplitude, which directly affects position and shape of the Dirac nodes.

In the following, we define Δ_{CT} as the energy difference between the average energy position of the full d manifold and the average one of the p manifold. According to our HSE calculations, Δ_{CT} varies from 1.1 eV ($x = 1$) to 1.6 eV ($x = 0$). Assuming a linear variation of Δ_{CT} and on-site energies upon Ni-content x, we are able to estimate $\Delta_{CT} = \Delta_{CT}(x)$ and, thus, predict the evolution of the band structure and Dirac states by interpolating between the $BaCoS_2$ and $BaNiS_2$ TB models. This evolution is reported in Fig. 4(b), while the actual Dirac states dynamics - represented by the behavior of both the **k** and energy position of the Dirac point as a function of Δ_{CT} - is plotted in Fig. 4(c). This shows that the tunability upon doping found experimentally does not merely consist of a rigid shift of the Dirac cones (19), but it involves the change of both their shape and **k**-position (see also Fig. S8).

This theoretical prediction is in good agreement with the observed evolution of the Dirac cone with x, as apparent in Fig. 4(a). Such movable Dirac nodes in the **k**-space have recently attracted a great deal of interest from theory (15, 28, 57), as well as in the context of optical lattices (25) and photonic crystals (26). The present system offers the opportunity of observing in a real material how a simple experimental parameter - chemical substitution - can be used to tune Dirac states.

Manipulating the shape and position of the Dirac cones is also expected in $BaCo_{1-x}Ni_xS_2$ using pressure in bulk samples or strain in thin films. Specifically, strain can be used to distort the square lattice, thus breaking one of the symmetries that protect the fourfold Dirac nodal lines. Non-trivial phases, such as Weyl semimetals, could then be triggered by time-inversion breaking perturbations, like an external electromagnetic field. A further possibility is the creation of spin-chiral edge states thanks to the proximity of the material to a topological insulator.

Conclusion

In conclusion, we have shown that $BaCo_{1-x}Ni_xS_2$ offers the opportunity of effectively tuning Dirac bands by exploiting a peculiar inversion mechanism of d-electron bands. Namely, the Co/Ni substitution has been found to alter both the charge transfer gap and the strength of the electron-electron correlations that control position and shape of the bands. Remarkably, the same Co/Ni substitution makes it possible to span the electronic phase diagram, with the Dirac states present across its metallic phase. We emphasize the applicability of the present approach to a wide class of materials described by the $d-p$ effective Hamiltonian, thus enabling to forge new Dirac states controlled by chemical substitutions. This opens the perspective of engineering Dirac states in correlated electronic systems by exploiting macroscopically tunable parameters.

Materials and Methods

ARPES measurements. Single crystals of $BaCo_{1-x}Ni_xS_2$ were cleaved *in-situ*, exposing the *ab* plane under UHV conditions (base pressure better than 10^{-11} mbar). Most of the synchrotron radiation ARPES measurements were performed on the Advanced Photoelectric Effect (APE) beamline at the Elettra light source, with linearly polarized beam and different photon energies. The sample temperature was 70 K. The data were collected with a VG-DA30 Scienta hemispherical analyzer that operates in deflection mode and provides high-resolution two-dimensional **k**-space mapping while the sample geometry is fixed (58). The total measured energy resolution is $\sim$ 15 meV and the angular resolution is better than 0.2°. Some of the data were also acquired with a 6.2 eV laser source (59); and some at the Spectromicroscopy beamline (60): the end station hosts two exchangeable multilayer-coated Schwarzschild objectives (SO) designed to focus the radiation at 27 eV and 74 eV to a small spot ($\sim$600 nm). The photoelectrons are collected by an internal movable hemispherical electron energy analyzer that can perform polar and azimuthal angular scans in UHV. The energy and momentum resolutions are $\sim$33 meV and $\sim$0.03 Å^{-1}, respectively.

***Ab initio* calculations.** We carried out *ab initio* DFT calculations in a modified HSE functional. It improves upon the Perdew, Burke, and Ernzerhof (PBE) (61, 62) exchange-correlation (xc) functional by the addition of a screened Fock term ($E_x^{HF,\text{screened}}$), such that the resulting functional reads as

$$E_{xc}^{HSE} = E_{xc}^{PBE} + \alpha \left(E_x^{HF,\text{screened}}(\omega) - E_x^{PBE,\text{screened}}(\omega) \right). \quad [1]$$

The screened interaction is written as: $V^{\text{screened}}(r) = \text{erfc}(\omega r)/r$, where erfc is the complementary error function, and $\omega = 0.108$ in atomic units, *i.e.* the HSE regular value. In this work, α is instead taken as an adjustable parameter, which depends on the correlation strength of the system.

We used the Quantum Espresso package (63, 64) to perform modified HSE calculations for $BaNiS_2$ ($x = 1$) and $BaCoS_2$ ($x = 0$) in a plane-waves (PW) basis set. The geometry of the cell and the internal coordinates are taken from experiment (45). We replaced the core electrons of the Ni, Co, Ba, and S atoms by norm-conserving pseudopotentials. For the Ni (Co) pseudopotential, we used both fully- and scalar-relativistic versions, with 10 (9) valence electrons and nonlinear core corrections. The Ba pseudopotential includes the semicore states, while the S pseudopotential has $3s^2 3p^4$ valence electrons. We employed a $8 \times 8 \times 8$ electron-momentum grid and a Methfessel-Paxton smearing of 0.01 Ry for the **k**-point integration. The PW cutoff is 60 Ry for the wave function. The non-local exchange terms of the HSE functional are computed through the fast implementation of the exact Fock energy (64), based on the adaptively compressed exchange scheme (65). In the non-local Fock operator evaluation, the integration over the **q**-points is downsampled on a $8 \times 8 \times 2$ grid. We applied a half-a-grid shift in the z direction to minimize the number of nonequivalent momenta in the $\mathbf{k} + \mathbf{q}$ grid. By means of the Wannier90 code (66), we performed a Wannier interpolation of the *ab initio* bands for $x = 1$ in the energy window spanned by the $d-p$ manifold, to accurately resolve the band structure, chemical potential, and Fermi surface, and to derive a minimal TB model.

To successfully deal with the most demanding simulations (HSE functional evaluated in a larger cell with spin resolved orbitals), we supplemented the Quantum Espresso calculations with some performed by means of the Crystal17 package(67), particularly suited to efficiently compute the exact exchange operator. In this framework, we used scalar-relativistic Hartree-Fock energy-consistent pseudopotentials by Burkatzki, Filippi, and Dolg(68), and an adapted VTZ Gaussian basis set, for both Ni and Co. In our Crystal17 calculations, the k-grid has been set to a $32 \times 32 \times 32$ dense mesh, with a Fermi smearing of 0.001 Hartree. We cross-checked the Crystal17 and Quantum Espresso band structures for the paramagnetic phase of $BaNiS_2$ and $BaCoS_2$, in order to verify the convergence of all relevant parameters in both PW and Gaussian DFT calculations.

ACKNOWLEDGMENTS. This work was supported by "Investissement d'Avenir" Labex PALM (ANR-10-LABX-0039-PALM), by the Region Ile-de-France (DIM OxyMORE), and by the project CALIPSOplus under Grant Agreement 730872 from the EU Framework Programme for Research and Innovation HORIZON 2020. We acknowledge Benoît Baptiste for XRD characterization and Imène

Estève for her valuable assistance in the EDS study. M.C. is grateful to GENCI for the allocation of computer resources under the project N. 0906493. M.F. and A.A. acknowledge support by the European Union, under ERC AdG "FIRSTORM", contract N. 692670.

1. MZ Hasan, CL Kane, Colloquium: Topological insulators. *Rev. Mod. Phys.* **82**, 3045 (2010).
2. A Bansil, H Lin, T Das, Colloquium: Topological band theory. *Rev. Mod. Phys.* **88**, 021004 (2016).
3. B Bradlyn, et al., Topological quantum chemistry. *Nature* **547**, 298–305 (2017).
4. NP Armitage, EJ Mele, A Vishwanath, Weyl and Dirac semimetals in three-dimensional solids. *Rev. Mod. Phys.* **90**, 15001 (2018).
5. QD Gibson, et al., Three-dimensional Dirac semimetals: Design principles and predictions of new materials. *Phys. Rev. B* **91**, 205128 (2015).
6. MG Vergniory, et al., A complete catalogue of high-quality topological materials. *Nature* **566**, 480–485 (2019).
7. Z Wang, et al., Dirac semimetal and topological phase transitions in A_3Bi (A=Na, K, Rb). *Phys. Rev. B* **85**, 195320 (2012).
8. S Borisenko, et al., Experimental Realization of a Three-Dimensional Dirac Semimetal. *Phys. Rev. Lett.* **113**, 027603 (2014).
9. ZK Liu, et al., A stable three-dimensional topological Dirac semimetal Cd_3As_2. *Nat. Mater.* **13**, 677–681 (2014).
10. L Müchler, et al., Topological Insulators from a Chemist's Perspective. *Angew. Chemie* **51**, 7221–7225 (2012).
11. CL Kane, EJ Mele, Z_2 Topological Order and the Quantum Spin Hall Effect. *Phys. Rev. Lett.* **95**, 146802 (2005).
12. SM Young, et al., Dirac Semimetal in Three Dimensions. *Phys. Rev. Lett.* **108**, 140405 (2012).
13. SM Young, CL Kane, Dirac Semimetals in Two Dimensions. *Phys. Rev. Lett.* **155**, 126803 (2015).
14. L Muechler, A Alexandradinata, T Neupert, R Car, Topological Nonsymmorphic Metals from Band Inversion. *Phys. Rev. X* **6**, 041069 (2016).
15. BJ Yang, N Nagaosa, Classification of stable three-dimensional Dirac semimetals with nontrivial topology. *Nat. Commun.* **5**, 4898 (2014).
16. M Yan, et al., Lorentz-violating type-II Dirac fermions in transition metal dichalcogenide $PtTe_2$. *Nat. Commun.* **8**, 1–6 (2017).
17. H Hübener, MA Sentef, U De Giovannini, AF Kemper, A Rubio, Creating stable Floquet-Weyl semimetals by laser-driving of 3D Dirac materials. *Nat. Commun.* **8**, 13940 (2017).
18. MS Bahramy, et al., Ubiquitous formation of bulk Dirac cones and topological surface states from a single orbital manifold in transition-metal dichalcogenides. *Nat. Mater.* **17**, 21–28 (2018).
19. F Fei, et al., Band Structure Perfection and Superconductivity in Type-II Dirac Semimetal $Ir_{1-x}Pt_xTe_2$. *Adv. Mater.* **30**, 1801556 (2018).
20. Y Cao, et al., Unconventional superconductivity in magic-angle graphene superlattices. *Nature* **556**, 43–50 (2018).
21. Y Cao, et al., Correlated Insulator Behaviour at Half-Filling in Magic Angle Graphene Superlattices. *Nature* **556**, 80–84 (2018).
22. L Ye, et al., Massive Dirac fermions in a ferromagnetic kagome metal. *Nature* **555**, 638–642 (2018).
23. JX Yin, et al., Giant and anisotropic many-body spin–orbit tunability in a strongly correlated kagome magnet. *Nature* **562**, 91–95 (2018).
24. X Qian, J Liu, L Fu, J Li, Quantum spin Hall effect in two-dimensional transition metal dichalcogenides. *Science* **346**, 1344–1347 (2014).
25. L Tarruell, D Greif, T Uehlinger, G Jotzu, T Esslinger, Creating, moving and merging Dirac points with a Fermi gas in a tunable honeycomb lattice. *Nature* **483**, 302–305 (2012).
26. M Milićević, et al., Type-III and tilted Dirac cones emerging from flat bands in photonic orbital graphene. *Phys. Rev. X* **9**, 031010 (2019).
27. G Montambaux, LK Lim, JN Fuchs, F Piéchon, Winding vector: how to annihilate two Dirac points with the same charge. *Phys. Rev. Lett.* **121**, 256402 (2018).
28. M Gonçalves, P Ribeiro, EV Castro, Dirac points merging and wandering in a model Chern insulator. *EPL (Europhysics Lett.)* **124**, 67003 (2019).
29. Hübener, Hannes and De Giovannini, Umberto and Schäfer, Christian and Andberger, Johan and Ruggenthaler, Michael and Faist, Jerome and Rubio, Angel, Engineering quantum materials with chiral optical cavities. *Nat. Mater.* **20**, 438–442 (2020).
30. DM Kennes, et al., Moiré heterostructures: a condensed matter quantum simulator. *Nat. Phys.* **17**, 155–163 (201).
31. S Pakhira, JL Mendoza-Cortes, Tuning the Dirac cone of bilayer and bulk structure graphene by intercalating first row transition metals using first-principles calculations. *J. Phys. Chem. C* **122**, 4768–4782 (2018).
32. Y Tsujikawa, et al., Controlling of the Dirac band states of Pb-deposited graphene by using work function difference. *AIP Adv.* **10**, 085314 (2020).
33. S Roy, et al., Tuning the Dirac Point Position in Bi_2Se_3 (0001) via Surface Carbon Doping. *Phys. Rev. Lett.* **113**, 116802 (2014).
34. L Miao, et al., Observation of a topological insulator Dirac cone reshaped by non-magnetic impurity resonance. *npj Quantum Mater.* **3**, 1–7 (2018).
35. D Galanakis, TD Stanescu, Electrostatic effects and band bending in doped topological insulators. *Phys. Rev. B* **86**, 195311 (2012).
36. A Díaz-Fernández, L Chico, J González, F Domínguez-Adame, Tuning the Fermi velocity in Dirac materials with an electric field. *Sci. Reports* **7**, 1–8 (2017).
37. A Díaz-Fernández, E Díaz, A Gómez-León, G Platero, F Domínguez-Adame, Floquet engineering of Dirac cones on the surface of a topological insulator. *Phys. Rev. B* **100**, 075412 (2019).
38. B Zhou, et al., Controlling the carriers of topological insulators by bulk and surface doping. *Semicond. Sci. Technol.* **27**, 124002 (2012).
39. T Sato, et al., Evolution of metallic states from the Hubbard band in the two-dimensional Mott system $BaCo_{1-x}Ni_xS_2$. *Phys. Rev. B* **64**, 075103 (2001).
40. LS Martinson, JW Schweitzer, NC Baenziger, Metal-Insulator Transitions in $BaCo_{1-x}Ni_xS_{2-y}$. *Phys. Rev. Lett.* **71**, 125 (1993).
41. S Krishnakumar, T Saha-Dasgupta, N Shanthi, P Mahadevan, D Sarma, Electronic structure of and covalency driven metal-insulator transition in $BaCo_{1-x}Ni_xS_2$. *Phys. Rev. B* **63**, 045111 (2001).
42. D Mandrus, et al., Magnetism in $BaCoS_2$. *J. Appl. Phys.* **81**, 4620–4622 (1997).
43. D Santos-Cottin, et al., Linear behavior of the optical conductivity and incoherent charge transport in $BaCoS_2$. *Phys. Rev. Mater.* **2**, 105001 (2018).
44. D Santos-Cottin, et al., Anomalous metallic state in quasi-two-dimensional $BaNiS_2$. *Phys. Rev. B* **93**, 125120 (2016).
45. IE Grey, H Steinfink, Crystal Structure and Properties of Barium Nickel Sulfide, a Square-Pyramidal Nickel (II) Compound. *J. Am. Chem. Soc.* **92**, 5093 (1970).
46. Y Kim, BJ Wieder, CL Kane, AM Rappe, Dirac Line Nodes in Inversion-Symmetric Crystals. *Phys. Rev. Lett.* **115**, 036806 (2015).
47. R Yu, H Weng, Z Fang, X Dai, X Hu, Topological Node-Line Semimetal and Dirac Semimetal State in Antiperovskite Cu_3PdN. *Phys. Rev. Lett.* **115**, 036807 (2015).
48. LS Xie, et al., A new form of Ca_3P_2 with a ring of Dirac nodes. *APL Mater.* **3**, 083602 (2015).
49. LM Schoop, et al., Dirac cone protected by non-symmorphic symmetry and three-dimensional Dirac line node in ZrSiS. *Nat. Commun.* **7**, 11696 (2016).
50. N Nilforoushan, et al., Photoinduced renormalization and electronic screening of quasi-two-dimensional Dirac states in $BaNiS_2$. *Phys. Rev. Res.* **2**, 043397 (2020).
51. Y Klein, et al., Importance of nonlocal electron correlation in the $BaNiS_2$ semimetal from quantum oscillations studies. *Phys. Rev. B* **97**, 075140 (2018).
52. I Hase, N Shirakawa, Y Nishihara, Electronic structures of $BaNiS_2$ and $BaCoS_2$. *J. Phys. Soc. Jpn.* **64**, 2533–2540 (1995).
53. D Santos-Cottin, et al., Rashba coupling amplification by a staggered crystal field. *Nat. Commun.* **7**, 11258 (2016).
54. V Cvetkovic, O Vafek, Space group symmetry, spin-orbit coupling, and the low-energy effective Hamiltonian for iron-based superconductors. *Phys. Rev. B* **88**, 134510 (2013).
55. L de'Medici, J Mravlje, A Georges, Janus-Faced Influence of Hund's Rule Coupling in Strongly Correlated Materials. *Phys. Rev. Lett.* **107**, 256401 (2011).
56. P Liu, et al., Electron and hole doping in the relativistic Mott insulator Sr_2IrO_4: A first-principles study using band unfolding technique. *Phys. Rev. B* **94**, 195145 (2016).
57. D Carpentier, AA Fedorenko, E Orignac, Effect of disorder on 2D topological merging transition from a Dirac semi-metal to a normal insulator. *EPL (Europhysics Lett.* **102**, 67010 (2013).
58. C Bigi, et al., Very efficient spin polarization analysis (VESPA): New exchange scattering-based setup for spin-resolved ARPES at APE-NFFA beamline at Elettra. *J. Synchrotron Radiat.* **24**, 750–756 (2017).
59. M Caputo, et al., Dynamics of out-of-equilibrium electron and hole pockets in the type-II Weyl semi-metal candidate WTe_2. *Phys. Rev. B* **97**, 115115 (2018).
60. P Dudin, et al., Angle-resolved photoemission spectroscopy and imaging with a submicrometre probe at the SPECTROMICROSCOPY-3.2L beamline of Elettra. *J. Synchrotron Radiat.* **17**, 445–450 (2010).
61. JP Perdew, K Burke, M Ernzerhof, Generalized Gradient Approximation Made Simple. *Phys. Rev. Lett.* **77**, 3865 (1996).
62. K Perdew, J. P. Burke, M Ernzerhof, Generalized Gradient Approximation Made Simple [Phys. Rev. Lett. 77, 3865 (1996)]. *Phys. Rev. Lett.* **78**, 1396 (1996).
63. P Giannozzi, et al., QUANTUM ESPRESSO : a modular and open-source software project for quantum simulations of materials. *J. Phys. Condens. Matter* **21**, 395502 (2009).
64. P Giannozzi, et al., Advanced capabilities for materials modelling with Quantum ESPRESSO. *J. Physics: Condens. Matter* **29**, 465901 (2017).
65. L Lin, Adaptively Compressed Exchange Operator. *J. Chem. Theory Comput.* **12**, 2242 (2016).
66. AA Mostofi, et al., wannier90 : A tool for obtaining maximally-localised Wannier functions. *Comput. Phys. Commun.* **178**, 685–699 (2008).
67. R Dovesi, et al., Quantum-mechanical condensed matter simulations with CRYSTAL. *Wiley Interdiscip. Rev. Comput. Mol. Sci.* **8**, e1360 (2018).
68. M Burkatzki, C Filippi, M Dolg, nergy-consistent small-core pseudopotentials for 3d-transition metals adapted to quantum Monte Carlo calculations. *The J. chemical physics* **129**, 164115 (2008).